Revealing the Intrinsic Nanohardness of Lath Martensite in Low Carbon Steel

B.B. HE and M.X. HUANG

The mechanical property of martensite blocks in low carbon steel is studied by nanoindentation combined with scanning electron microscopy, electron backscattered diffraction, and transmission electron microscopy. The average nanohardnesses of small and large martensite blocks are 6.9 and 5.4 GPa, respectively. A size effect that the smaller is stronger is thus observed. This size effect was ascribed to the different formation sequence of martensite blocks during quenching. Therefore, the present work suggests that the as-quenched martensite may be considered as a composite material with the small but strong martensite blocks embedded in the large but soft martensite block matrix, which is important information for modeling the tensile stress–strain behavior of martensitic steel.

I. INTRODUCTION

LATH martensite, which contains high dislocation density and is also called "dislocated martensite,"[1] plays an important role in determining the mechanical properties of advanced high strength steel and martensitic steel. For instance, the recently developed quenching and partitioning steel[2,3] contains the lath martensite as the matrix to provide high strength. The morphologies of lath martensite in steels can be grouped into packet, block, and lath.[4,5] The packet is a group of blocks with the same habit plane, and a block contains laths with the same orientation.[4,5] The strength of low carbon martensitic steel was reported to change with the variation of martensite block size.[6] In other words, the block size may be considered as the "grain size" of martensite. The martensite block size can be refined by increasing the C or Mn content or by decreasing the prior austenite grain size.[4,6] The mechanical property of martensite block has been studied using the nanoindentation technique.[7–12] The intrinsic nanohardness of martensite block, which excludes the boundary effects, is mainly determined by dislocation strengthening, solid solution strengthening (including the interstitial C atoms), and precipitation strengthening. Such intrinsic nanohardness can be revealed by nanoindentation tests on the individual martensite blocks. Nevertheless, the intrinsic nanohardness of martensite block may be affected by the presence of densely distributed high-angle boundaries, which contain the prior austenite grain boundary (PAGB), packet boundary, and block boundary.[4,5] The high-angle boundary can stop the transmission of dislocation and confine the indentation plastic zone,

thus contributing to the nanohardness of martensite block, if the nanoindentation tests are close to the high-angle boundaries.[8,13] Therefore, avoiding the contribution of the high-angle boundary in order to obtain the intrinsic nanohardness of the martensite block is required. This can be realized through the postanalysis on the indentation impressions using scanning electron microscopy (SEM) and electron backscattered diffraction (EBSD) combined with the detailed analysis on the indentation load displacement (P–h) curve. The present work is aimed at revealing the intrinsic nanohardness of martensite block by using the combined techniques including nanoindentation, SEM, EBSD, and transmission electron microscopy (TEM).

II. EXPERIMENTAL PROCEDURES

Low carbon steel with a chemical composition of Fe-0.2C-1.5Mn-2Cr (in wt pct) was employed for the present study. The detailed material processing procedure can be found in a recent publication.[14] The full martensite microstructure was obtained by helium quenching in a dilatometer (Bähr, 805 A/D) after a homogenization at 1173 K (900 °C) for 300 seconds with a cooling rate of 100 °C/s. The average prior austenite grain size is about 15 μm. The sample for the nanoindentation test was prepared by electropolishing with a solution of 25 pct perchloric acid and 75 pct ethanol at room temperature after a mechanical finish of 1 μm. The nanoindentation tests were carried out using an Agilent Nano indenter G200 equipped with a Berkovich indenter with a half-angle of 65.3 deg at ambient temperature. The tip correction was performed on the fused silica. A maximum load of 3 mN was applied with the loading part finished in 10 seconds. The analysis on the P–h curve was based on the continuous stiffness method.[15] Four groups of indentation matrix, each of which contained 6×6 indents with a spacing of 2 μm, were performed on the prepared sample.

B.B. HE, Ph.D. Candidate, and M.X. HUANG, Assistant Professor, are with the Shenzhen Institute of Research and Innovation, University of Hong Kong, Shenzhen, P.R. China and also with the Department of Mechanical Engineering, University of Hong Kong, Hong Kong, P.R. China. Contact e-mail: mxhuang@hku.hk
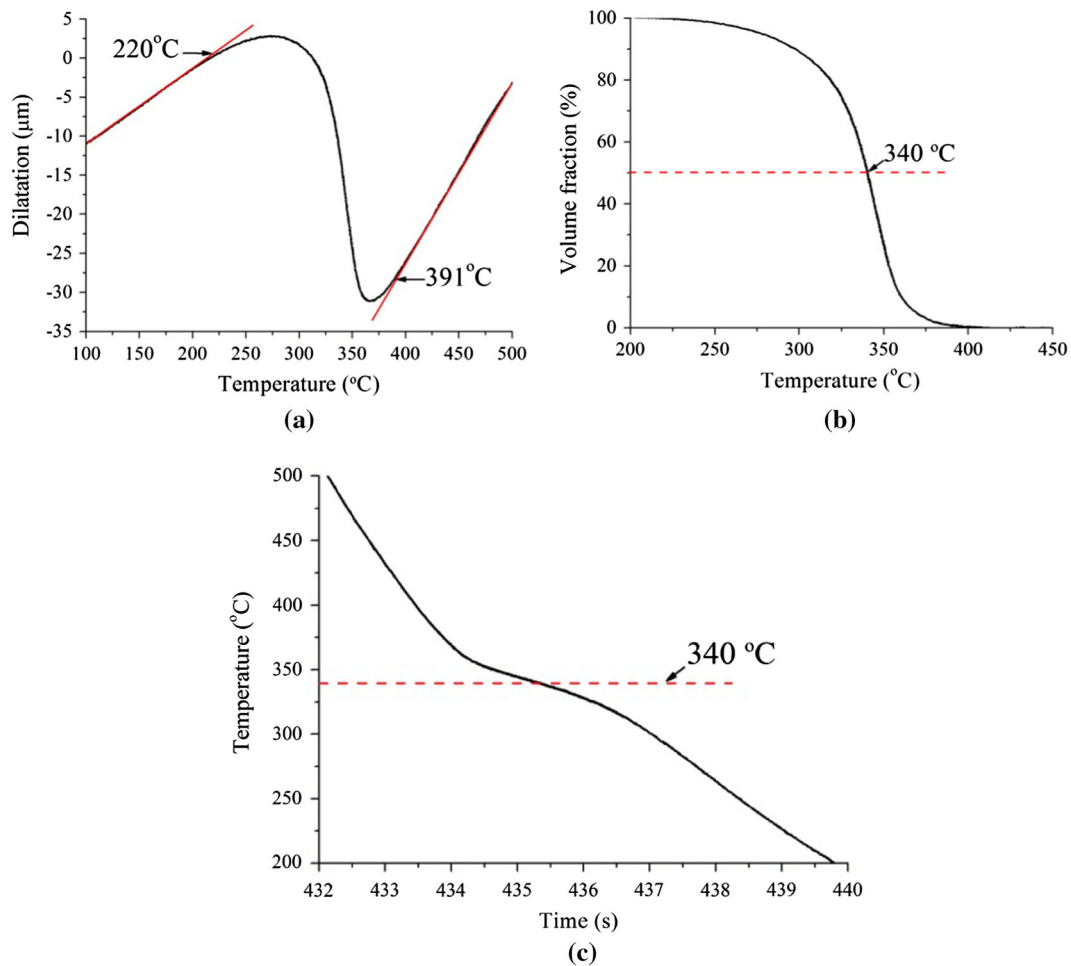
Fig. 1—(*a*) Dilatational signal during the martensitic transformation, (*b*) the martensitic transformation kinetics, and (*c*) the evolution of temperature during the continuous cooling process.

The postanalysis on the indentation impressions was performed using SEM at 5 kV (LEO 1530) and EBSD at 20 kV (HKL Channel 5). For the EBSD measurement, a step size of 0.1 μm was used. TEM experiments were carried out to identify the martensite lath width in a FEI Tecnai G20 at 200 kV. The TEM sample was prepared by mechanical thinning down to 0.07 mm using SiC paper. The small discs with diameter of 3 mm were punched from the thin small plate. A twin jet was employed to perforate the small discs using a mixture of 5 pct perchloric acid, 15 pct acetic acid, and 80 pct ethanol (vol pct) at −20 °C with a potential of 50 V.

III. RESULTS AND DISCUSSION

Figure 1(a) is the dilatational signal of martensitic transformation with a quenching rate of 100 °C/s. The martensite start (M_s) and martensite finish (M_f) temperatures are identified to be 664 K and 493 K (391 °C and 220 °C), respectively, using the tangent method.[16] The EBSD measurement confirmed the full martensite microstructure after quenching. Figure 1(b) is the martensitic transformation kinetics, which was extracted from the dilatational signal using the lever rule.[17] The martensitic transformation burst after the initial nucleation and 50 pct martensite volume fraction was obtained at 613 K (340 °C), which is only 51 °C lower than the M_s temperature. Figure 1(c) shows that the heat generated during the burst of martensitic transformation slowed the cooling rate from 100 to 20 °C/s. It is reasonable to estimate that the early transformed martensite has a higher possibility to be autotempered. This is confirmed from the existence of martensite blocks with different autotempered levels within a single prior austenite grain, as pointed out by arrows in Figure 2(a). Figure 2(b) is an enlarged view of the dashed rectangle in Figure 2(a), showing that some martensite blocks marked with a red rectangle have high lath boundary density and others have a high density of carbide precipitations. The martensite block may have different size within the same prior austenite grain. This is confirmed from the EBSD band contrast image, as shown in Figure 2(c). The earlier transformed martensite may have a larger size than the later transformed one, because it can transform across the whole austenite grain and the later transformed martensite has to transform within the smaller austenite grain size after
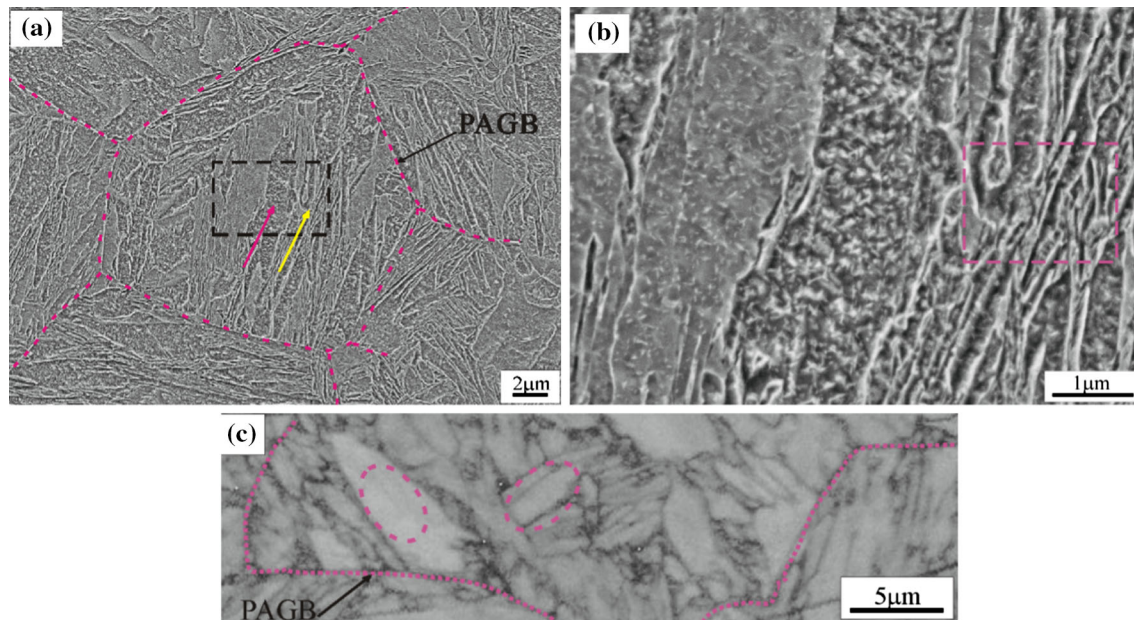
Fig. 2—(*a*) SEM image of lath martensite in the present steel. The PAGB is discernible. The autotempered martensite is marked with a red arrow, and the as-quenched martensite is marked with a yellow arrow. (*b*) The magnified view of the dashed box in (a). The dashed box marks the densely distributed lath boundaries in the prior austenite grain. (*c*) EBSD band contrast image showing the existence of both large and small martensite blocks within the prior austenite grain.

Table I. Information of K–S Variants in Packet 1[19,20]

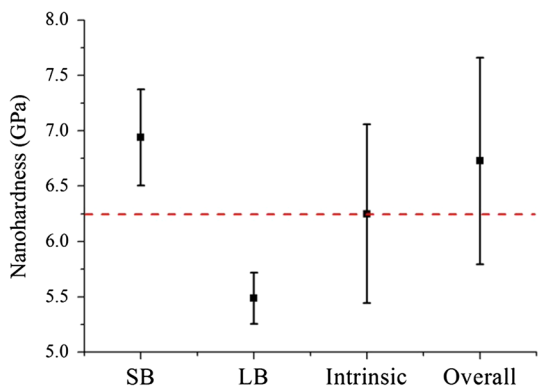| Variant	Parallel Planes	Parallel Directions	Misorientation Angle/Axis from V1
V1	$(111)\gamma\|(011)\alpha'$	$[-101]\gamma\|[-1-11]\alpha'$	—
V2	$(111)\gamma\|(011)\alpha'$	$[-101]\gamma\|[-11-1]\alpha'$	60.00/[11-1]α'
V3	$(111)\gamma\|(011)\alpha'$	$[01-1]\gamma\|[-1-11]\alpha'$	60.00/[011]α'
V4	$(111)\gamma\|(011)\alpha'$	$[01-1]\gamma\|[-1-11]\alpha'$	10.53/[0-1-1]α'
V5	$(111)\gamma\|(011)\alpha'$	$[1-10]\gamma\|[-1-11]\alpha'$	60.00/[0-1-1]α'
V6	$(111)\gamma\|(011)\alpha'$	$[1-10]\gamma\|[-11-1]\alpha'$	49.47/[011]α'

Fig. 3—Nanohardness of martensite in the present low carbon steel. SB: small martensite block; LB: large martensite block. The intrinsic nanohardness is the average nanohardness of both small and large martensite blocks. The overall nanohardness is obtained by averaging over all the data points. The error bar represents the standard deviation of at least 10 data points.

Reports indicate that the orientation relationship between parent austenite and product martensite is close to the Kurdjumov–Sachs (K–S) orientation relationship in a low carbon steel.[18] So the K–S orientation relationship is assumed here. According to the K–S orientation relationship, the prior austenite grain shall contain 24 equivalent crystallographic martensite variants, which can be grouped into four packets each containing six variants sharing the same habit plane. Table I shows the crystallographic information of six martensite variants in packet 1.[19,20] The two martensite variants with the same orientation comprise one martensite block. As shown in Table I, three martensite blocks (V1/V4, V2/V5, and V3/V6) are found in packet 1. The block boundaries have misorientation angles that vary between 49.47 and 60 deg in packet 1, so they are considered as the high-angle boundaries. On the other hand, the lath boundaries are the low-angle boundaries with a low misorientation of about 10.53 deg.

Figure 3 shows that the small martensite block has a higher nanohardness than the large martensite block. The differentiation of martensite blocks is by SEM and EBSD images. It is noted that the sizes of the large and small blocks are estimated to be about 6 and 3.5 μm,
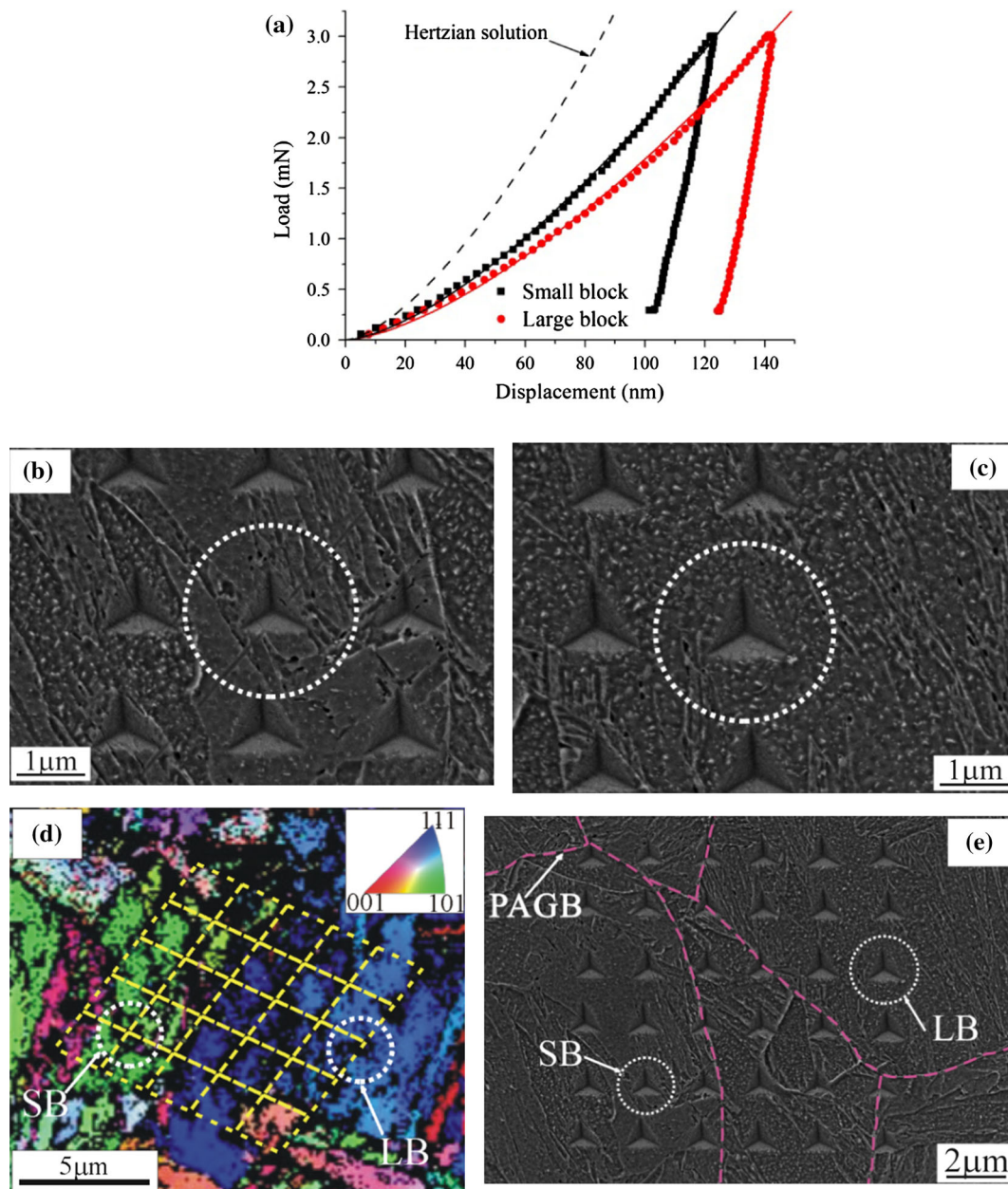
the initial geometrical partitioning. In other words, the large martensite block, as shown in Figure 2(c), may transform earlier than the small martensite block and, thus, be subjected to greater autotempering.

Fig. 4—(a) P–h curves of the indentations at small and large martensite blocks with the fitting using Hertzian solution and GND concept. (b) SEM image of small martensite block. (c) SEM image of large martensite block. (d) EBSD inverse pole figure showing the interested indents are within the martensite blocks. (e) Corresponding SEM image showing the distribution of 36 indentation impressions. The interested indents are within the white dashed circles. The color images can be obtained in the online version of this article.

respectively, from the EBSD orientation images. The size of the indentation impression is about 1 to 1.3 μm, which is small enough as compared to the size of both small and large martensite blocks. The effect of high-angle boundaries, including the PAGB, packet boundary, and block boundary, is excluded by neglecting the nanohardness of indents close to the high-angle boundaries. The overall nanohardness shown in Figure 3 is the average nanohardness of all nanoindentation tests, which includes the tests inside the martensite blocks and those close to the high-angle boundaries. Figure 3 shows that the overall nanohardness is about 0.5 GPa

higher than the intrinsic nanohardness under the maximum load of 3 mN.

Figure 4(a) shows the typical P–h curves of indents on the small and large martensite blocks. Figures 4(b) and (c) show the corresponding indentation impressions at small and large martensite blocks, respectively. It can be found from Figures 4(b) and (c) that the indent size is about 1 μm at an interdistance of about 1 μm. The pileup in the periphery of the indentation impression is small so that it will not affect the neighboring indents. Moreover, it will be shown later that the radius of the effective plastic zone is only about 1.2 times that of the
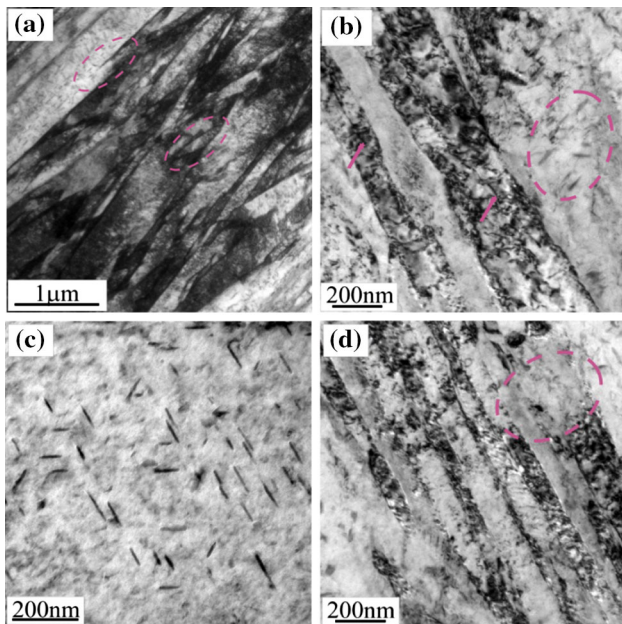
Fig. 5—(a) TEM bright-field image showing the varied martensite lath width in the present steel. (b) TEM bright-field image showing the high dislocation density in narrow martensite lath. Red arrows point to the ending of the martensite lath boundary. The dashed circle marks the carbide precipitation in the wide martensite lath. (c) TEM bright-field image showing the densely distributed carbides in the wide martensite lath. No lath boundary is observed. (d) TEM bright-field image of lath martensite illustrating the diminishing martensite lath boundaries.

contact radius for large martensite block. By considering the present indent size and the interdistance, one may expect that the influence of the former indents on the latter indents should be quite small and may be neglected. Figure 4(d) is the EBSD inverse pole figure, confirming that the interested indentation impressions marked with the dashed circles are within the martensite blocks. Figure 4(e) shows the 36 indentation impressions, where those of interest are marked with dashed circles.

The elastic deformation of lath martensite during the indentation test can be analyzed by the Hertzian elastic contact solution, which reads[21]

$$P = \frac{4}{3} E_r R_i^{\frac{1}{2}} h^{\frac{3}{2}} \qquad [1]$$

and

$$\frac{1}{E_r} = \frac{1 - v_i^2}{E_i^2} + \frac{1 - v_s^2}{E_s^2} \qquad [2]$$

where the tip radius R_i is taken as 200 nm. The term E_r is the effective indentation modulus. The subscripts i and s represent the indenter and specimen, respectively. The Young's modulus E and Poisson's ratio v for the indenter and the specimen are 1140 GPa, 0.07,[22] and 220 GPa, 0.3,[23] respectively. The dashed line in Figure 3(a) is the Hertzian solution calculated from Eq. [1]. The deviation of P–h curves from the Hertzian solution is free from pop-in for both small and large martensite blocks. This may be due to the high dislocation density

within lath martensite so that it is highly possible that the indented volume contains pre-existing dislocations.[24,25]

The plastic part of the P–h curve can be fitted with the concept of geometry necessary dislocation (GND) as follows:[26]

$$P = A_c M C \beta G b \sqrt{\rho_{\text{SSD}} + \rho_{\text{GND}}} \qquad [3]$$

and

$$\rho_{\text{GND}} = \frac{3}{2} \frac{1}{f^3} \frac{\tan^2 \theta}{bh} \qquad [4]$$

where $A_c = 24.5\ h^2$ is the projected area for an ideal Berkovich indenter, M is the Taylor factor and is taken as 3 for the present material, $C = 3$ is a constraint factor, β is a value that represents the dislocation structure and is assumed to be 0.5, G is the shear modulus of martensite, $b = 0.286$ nm is the Burgers vector for martensite, ρ_{SSD} is the statistically stored dislocation density in the indentation plastic zone but is not considered here due to the low indentation depth (~130 nm),[26] ρ_{GND} is the GND density in the plastic zone, f is the ratio of the radius of the plastic zone a_{pz} to the contact radius a_c, and θ is the angle between the indenter and specimen surface. The fitting curves using the GND concept to the P–h curves are shown in Figure 4(a). The best fitting gives the values of f for the large and small martensite blocks as 1.2 and 1.05, respectively. A higher value of f represents a lower GND density within the plastic zone[8] so that the large martensite block has a lower nanohardness than the small martensite block. The small martensite block where the indent locates has densely distributed lath boundaries and is almost free of carbides (Figure 4(b)). On the other hand, the large martensite block where the indent locates is almost free of lath boundary but has high carbide density (Figure 4(c)). Further insights into the martensite microstructure may be obtained from TEM measurements. Figure 5(a) shows the TEM bright-field image of both large and small martensite blocks, where the martensite lath width is varied between 0.1 and 0.5 μm. It is thus reasonable to estimate that lath boundary density is varied in the present lath martensite. Figure 5(b) shows that the narrow martensite lath (~0.13 μm) within a small martensite block has a high dislocation density and that the wider martensite lath within a large martensite block has a high density of carbide precipitation (dashed ellipse). Figure 5(c) further illustrates that the wide martensite lath (~0.6 μm), which is within a large martensite block, has a relatively lower dislocation density but has a higher density of carbide with a width of about 10 nm. The carbide is not coarsened due to the short time of autotempering (Figure 1(c)). Since the prior austenite grain size has little effect on the martensite lath width,[27] the variation of martensite lath width, as observed in Figure 5(a), may be due to the autotempering effect. The earlier transformed martensite block is generally larger than the later transformed one. The martensite lath boundaries are low-angle boundaries (~10.53 deg), which may be
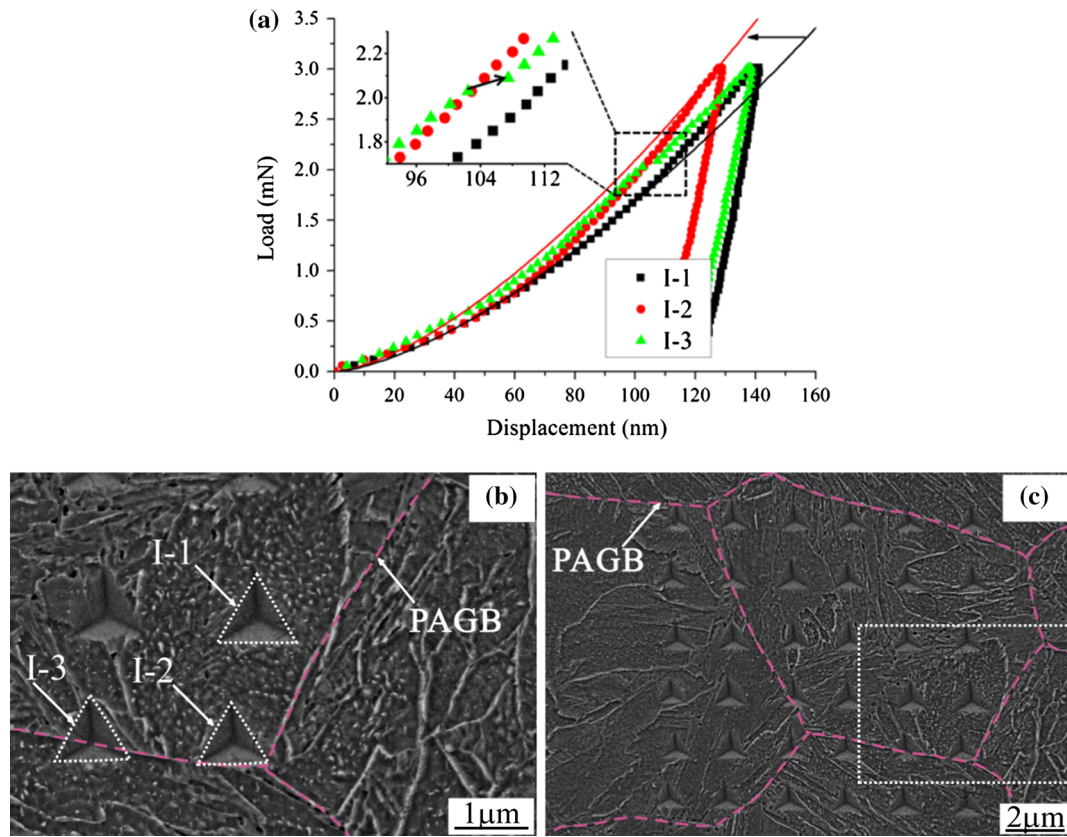
Fig. 6—(a) P–h curves of the indentations with fitting using the GND concept. (b) SEM image showing the location of three indentation impressions. (c) SEM image showing the distribution of 36 indentation impressions. The inset in (a) shows the pop-in in the P–h curve of I-3.

modeled as arrays of dislocations.[4,28] The recovery of dislocation during autotempering may lead to the disappearance of martensite lath boundary, resulting in wide martensite lath in large martensite block (Figures 5(b) and (c)). The later transformed martensite is less autotempered, so the lath boundary is still clear and observable (Figure 5(b)). This hypothesis may be supported by the evidence, as shown in Figure 5(d), that part of the lath boundaries within the circled area disappeared while the other lath boundaries remained within a small martensite block. Furthermore, the trace of the lath boundary is visible in Figure 5(b) and its ends are marked with red arrows. The autotempering leads to the weakening of three strengthening mechanisms, namely, dislocation strengthening, solid solution strengthening, and lath boundary strengthening. However, they were replaced by precipitation strengthening. The nanohardness of the large martensite block is obviously lower than that of the small martensite block (Figure 3), confirming that precipitation strengthening alone is not able to compensate for the loss of strength due to autotempering. The intrinsic nanohardness of the martensite block has a large standard deviation in the present steel. The present work suggests that it should be due to the different autotempering levels of lath martensite resulting from the different formation sequences of martensite blocks.

The overall nanohardness is larger than the intrinsic nanohardness (Figure 3). This may be due to the effect of the high-angle boundary. Figure 6(a) shows the P–h

curves of three indents marked I-1, I-2, and I-3. The corresponding indentation impressions are shown in Figure 6(b). Figure 6(c) shows the location of these three indents at the prior austenite grain. It is noted that I-2 is closer to the PAGB than I-1 and I-3 is the closest one to the PAGB. The fitting curves using the GND concept to the P–h curves of I-1 and I-2 are only successful at a displacement below 70 and 110 nm, respectively. This is different from the observation in Figure 4(a), where an excellent fitting is obtained. The value of f decreases from 1.25 to 1.08 for I-2 with the increase of indentation displacement, suggesting an increased effect of PAGB on confining the propagation of GNDs. The deviation of P–h curves from fitting curves in Figure 6(a) may be due to the significant deviation of the indentation plastic zone from the morphology of the hemisphere at high displacement, which results from the confinement of the PAGB on the propagation of GNDs. Since I-3 is the closest one to the PAGB, the penetration of the indenter at I-3 requires a higher load than both that of I-1 and I-2 at the initial loading stage (Figure 6(a)). However, the closeness of I-3 to the PAGB does not necessary provide it with the highest nanohardness among these three indentation tests. The P–h curve of I-3 shows a pop-in (inset of Figure 6(a)), and the other two P–h curves are free from pop-in. This pop-in may be due to the transmission of GNDs across the PAGB, since it leads to a softening of material.[29,30] The PAGB, which acts as a barrier for the dislocation transmission, may be destroyed by the

indenter or a critical stress for the dislocation transmission may be reached. The resultant nanohardness of the I-3 is only slightly higher than that of the I-1. It can be concluded that the high-angle boundary contributes to the nanohardness of martensite, depending on the distance of indents to the high-angle boundary. This conclusion will also apply to the packet and block boundaries, since they are also high-angle boundaries.

IV. CONCLUSIONS

In summary, using the nanoindentation technique and detailed microscopy analysis, the intrinsic nanohardness of martensite in low carbon steel has been revealed. Interestingly, this intrinsic nanohardness varies among the martensite blocks with different size. The small martensite block has a higher nanohardness than the large martensite block. In other words, the phenomenon that the smaller is stronger is observed in the as-quenched lath martensite. This size effect may be due to the different formation sequence of martensite blocks. The strengthening effect of the high-angle boundary on the nanohardness is observed, and it depends on the distance of indents to the high-angle boundary. The present work suggests that the present as-quenched martensite may be considered as a composite material with the small but strong martensite blocks embedded in the large but soft martensite blocks, which is important information for modeling the tensile stress–strain behavior of martensitic steel.

REFERENCES

1. L. Qi, A.G. Khachaturyan, and J.W. Morris: *Acta Mater.*, 2014, vol. 76, pp. 23–39.
2. X.C. Xiong, B. Chen, M.X. Huang, J.F. Wang, and L. Wang: *Scripta Mater.*, 2013, vol. 68, pp. 321–24.
3. J. Speer, D.K. Matlock, B.C. De Cooman, and J.G. Schroth: *Acta Mater.*, 2003, vol. 51, pp. 2611–22.
4. S. Morito, H. Tanaka, R. Konishi, T. Furuhara, and T. Maki: *Acta Mater.*, 2003, vol. 51, pp. 1789–99.
5. S. Morito, X. Huang, T. Furuhara, T. Maki, and N. Hansen: *Acta Mater.*, 2006, vol. 54, pp. 5323–31.
6. S. Morito, H. Yoshida, T. Maki, and X. Huang: *Mater. Sci. Eng., A*, 2006, vol. 438, pp. 237–40.
7. T. Ohmura, K. Tsuzaki, and S. Matsuoka: *Scripta Mater.*, 2001, vol. 45, pp. 889–94.
8. B.B. He, K. Zhu, and M.X. Huang: *Philos. Mag. Lett.*, 2014, pp. 1–8.
9. C. Ohlund, E. Schlangen, and S.E. Offerman: *Mater. Sci. Eng., A*, 2013, vol. 560, pp. 351–57.
10. T. Ohmura, K. Tsuzaki, and S. Matsuoka: *Philos. Mag. A*, 2002, vol. 82, pp. 1903–10.
11. T. Ohmura, T. Hara, and K. Tsuzaki: *Scripta Mater.*, 2003, vol. 49, pp. 1157–62.
12. T. Ohmura, T. Hara, and K. Tsuzaki: *J. Mater. Res.*, 2003, vol. 18, pp. 1465–70.
13. T. Ohmura, A.M. Minor, E.A. Stach, and J.W. Morris: *J. Mater. Res.*, 2004, vol. 19, pp. 3626–32.
14. B.B. He, W. Xu, and M.X. Huang: *Mater. Sci. Eng., A*, 2014, vol. 609, pp. 141–46.
15. W.C. Oliver and G.M. Pharr: *J. Mater. Res.*, 1992, vol. 7, pp. 1564–83.
16. Y.C. Liu, F. Sommer, and E.J. Mittemeijer: *Acta Mater.*, 2003, vol. 51, pp. 507–19.
17. T.A. Kop, J. Sietsma, and S. Van Der Zwaag: *J. Mater. Sci.*, 2001, vol. 36, pp. 519–26.
18. H.K.D.H. Bhadeshia and R. Honeycombe: *Steels: Microstructure and Properties*, 3rd ed., Butterworth-Heinemann, Oxford, 2006.
19. H. Kitahara, R. Ueji, N. Tsuji, and Y. Minamino: *Acta Mater.*, 2006, vol. 54, pp. 1279–88.
20. B.B. He, M.X. Huang, A.H.W. Ngan, and S. Van Der Zwaag: *Metall. Mater. Trans. A*, 2014, vol. 45A, pp. 4875–81.
21. K.L. Johnson: *Contact Mechanics*, Cambridge University Press, Cambridge, 1985.
22. S. Shim, H. Bei, E.P. George, and G.M. Pharr: *Scripta Mater.*, 2008, vol. 59, pp. 1095–98.
23. F. Lani, Q. Furnémont, T. Van Rompaey, F. Delannay, P.J. Jacques, and T. Pardoen: *Acta Mater.*, 2007, vol. 55, pp. 3695–3705.
24. A. Barnoush: *Acta Mater.*, 2012, vol. 60, pp. 1268–77.
25. G. Miyamoto, A. Shibata, T. Maki, and T. Furuhara: *Acta Mater.*, 2009, vol. 57, pp. 1120–31.
26. K. Durst, B. Backes, O. Franke, and M. Göken: *Acta Mater.*, 2006, vol. 54, pp. 2547–55.
27. S. Morito, H. Saito, T. Ogawa, T. Furuhara, and T. Maki: *ISIJ Int.*, 2005, vol. 45, pp. 91–94.
28. W.T. Read and W. Shockley: *Phys. Rev.*, 1950, vol. 78, pp. 275–89.
29. W.A. Soer, K.E. Aifantis, and J.T.M. De Hosson: *Acta Mater.*, 2005, vol. 53, pp. 4665–76.
30. B.B. He, M.X. Huang, Z.Y. Liang, A.H.W. Ngan, H.W. Luo, J. Shi, W.Q. Cao, and H. Dong: *Scripta Mater.*, 2013, vol. 69, pp. 215–18.